

Article

Historical aerial surveys map long-term changes of forest cover and structure in the central Congo Basin

Koen Hufkens^{1,2,*}, Thalès de Haulleville³, Elizabeth Kearsley¹, Kim Jacobsen^{1,3}, Hans Beeckman³, Piet Stoffelen⁴, Filip Vandelook⁴, Sofie Meeus⁴, Michael Amara⁵, Leen Van Hirtum⁵, Jan Van den Bulcke¹, Hans Verbeeck¹, Lisa Wingate²

¹ Ghent University, Ghent, Belgium;

² INRA, UMR ISPA, Villeneuve d'Ornon, France;

³ Royal Museum for Central Africa, Tervuren, Belgium;

⁴ Botanic Garden Meise, Meise, Belgium;

⁵ National Archives of Belgium, Brussels, Belgium;

* Correspondence: koen.hufkens@gmail.com

Version February 9, 2020 submitted to Remote Sens.



1 Abstract: Given the impact of tropical forest disturbances on atmospheric carbon emissions,
2 biodiversity and ecosystem productivity, accurate long term reporting of Land-Use and Land-Cover
3 (LULC) change in the pre-satellite era (< 1972) is an imperative. Here, we used a combination
4 of historical (1958) aerial photography and contemporary remote sensing data to map long-term
5 changes in the extent and structure of the tropical forest surrounding Yangambi (DR Congo), in
6 the central Congo Basin. Our study leveraged Structure-from-Motion and a Convolutional Neural
7 Network based LULC classifier, using synthetic landscapes based image augmentation, to map
8 historical forest cover across a large orthomosaic (~93 431 ha) geo-referenced to ~4.7 ± 4.3 m at sub
9 meter resolution. A comparison with contemporary LULC data showed a shift from previously
10 highly regular industrial deforestation of large areas, to discrete smallholder farming clearing,
11 increasing landscape fragmentation but also providing opportunities for substantial forest regrowth.
12 We estimated above ground carbon gains through reforestation to range from 811 to 1592 Gg C,
13 partially offsetting historical deforestation (2416 Gg C), in our study area. Efforts to quantify long
14 term canopy texture changes and their link to above ground carbon had limited to no success. Our
15 analysis provides methods and insights into key spatial and temporal patterns of deforestation and
16 reforestation at a multi-decadal scale, providing a historical context for past and ongoing forest
17 research in the area.

18 Keywords: Aerial survey, data recovery, CNN, Deep Learning, SfM, Congo Basin

19 1. Introduction

20 Tropical ecosystem services are severely impacted by deforestation and forest degradation [1–3].
21 Not only does tropical forest Land-Use and Land-Cover Change (LULCC) constitute 10 to 15% of
22 the total global carbon emissions [4], changes in forest fragmentation affect the forest structure and
23 function [5–7]. Strong fragmentation effects decrease the number of large trees along forest edges [8,9],
24 while species composition and biodiversity are equally negatively affected [10–12]. Estimates show
25 that 31% of carbon emissions are caused by edge effects alone [6].

26 Accurate estimates of LULCC and forest canopy structure are therefore imperative to estimate
27 carbon emissions and other ecosystem services [1,2]. Remote sensing products have been key inputs in
28 LULCC assessments as they provide accurate spatial information to help estimate carbon emissions
29 [1,13]. More so, high resolution aerial images provide scientists tools to monitor forest extent, structure
30 and carbon emissions as canopy texture is linked to above ground biomass [14–16]. Yet, most of these
31 estimates are limited in time to recent decades [1,2,17,18].

32 Historical estimates of Land-Use and Land-Cover (LULC), in the pre-satellite era (< 1972), exist
33 but generally rely on non-spatially explicit data (i.e socio-economic data) [2,17,19,20]. Efforts have
34 been made to use other geo-spatial data sources such as historical maps [21], declassified CORONA
35 satellite surveillance data across the US and central Brazil [22] as well as aerial surveys in post World
36 War II Germany [23]. Survey data across the African continent is less common, inaccessible or both.
37 Some studies do exist, as Buitenwerf *et al.* [24] and Hudak and Wessman [25] used aerial survey images
38 to map vegetation changes in South African savannas, whilst Frankl *et al.* [26] and Nyssen *et al.* [27]
39 mapped the Ethiopian highlands of 1930s.

40 Across the central Congo Basin most of these historical images were collected within the context
41 of national cartographic efforts by the “Institut Géographique du Congo Belge” in Kinshasa (then
42 Léopoldville), DR Congo. Despite the existence of large archives of aerial survey imagery of African
43 rainforest (Figure 1, Appendix Figure 3), as of yet, no studies have valorized these data. The lack of a
44 consistent valorization effort is unfortunate as the African rainforest is the second largest on Earth and
45 covers ~630 million ha, representing up to 66 Pg of carbon storage [28], and currently loses forest at an
46 increasing pace [29]. Given the impact of LULCC on the structure and functioning of central African
47 tropical forests, and their influence on both carbon dynamics [30] and biodiversity [12], accurate long
48 term reporting of historical forest cover warrants more attention [21].

49 Here, we use a combination of historical aerial photography (1958) and contemporary remote
50 sensing data (2000–2018) to map long-term changes in the extent and structure of the tropical forest
51 surrounding Yangambi (DR Congo), in the central Congo Basin, effectively linking the start of the
52 anthropocene [31] with current assessments. Yangambi was, and remains, a focal center of forest

53 and agricultural research and development in the central Congo Basin. Past research in the region
54 allows for thorough assessment of LULCC from a multi-disciplinary point of view, confronting us
55 with complex deforestation and land-use patterns.

56 We leverage Structure-from-Motion to generate a large orthomosaic of historical imagery and
57 develop a Convolutional Neural Network based forest cover mapping approach, based upon a
58 semi-supervised generated dataset extensively leveraging data augmentation. Our methodology
59 aims to provide a historical insight into important LULCC spatial patterns in Yangambi, such as
60 fragmentation and edge complexity. We further contextualize the influence of changes in the forest's
61 life history on past and current research into Above Ground Carbon (AGC) storage [30] and biodiversity
62 [12] in the central Congo Basin. Our fast scalable mapping approach for historical aerial survey data,
63 using limited supervised input, would further support long-term land-use and land-cover change
64 analysis across the central Congo Basin.

65 2. Methods

66 2.1. Historical data acquisition

67 Data for the central Congo Basin region, surrounding Kisangani, were collected in several flights
68 during the dry season of 1958 and 1959 (from 8/01/1958 to 20/02/1958 and from 28/12/1958 to
69 9/01/1959 respectively, see Appendix Figure 1 - 2 and Appendix Table 1) to generate topographic
70 maps of the area, supervised by the "Institut Géographique du Congo Belge" in Kinshasa, DR Congo
71 (then Léopoldville). Black-and-White panchromatic images (0.4 - 0.9 μm) were gathered along flight
72 paths running mostly from west to east, between 09:00 and 11:00 local time. Along a flight path
73 continuous images were taken using a Wild Heerburg RC5a (currently Leica Geosystems) with an
74 Aviogon lens assembly (114.83mm / f 5.6, with a 90°view angle) resulting in square photo negatives
75 of 180 by 180 mm. Flights were flown at an average absolute altitude of ~5200 m above sea level,
76 covering roughly 18 530 km² at an approximate scale of 1/40 000. The use of the integrated autograph
77 system ensured timely acquisition of pictures with a precise overlap (~1/3) between images. This
78 large overlap between images together with flight parameters would allow post-processing, using
79 stereographs, to create accurate topographic maps. Original data from this campaign are stored in the
80 Royal Museum for Central Africa in Tervuren, Belgium (Figure 1, Appendix Figure 3).

81 2.2. Site selection

82 We prioritised flight paths and images that contained current day permanent sampling plots,
83 larger protected areas, and past agricultural and forest research facilities (Figure 2). This selection
84 provides a comprehensive mapping of the Yangambi area and the life history of the forest surrounding

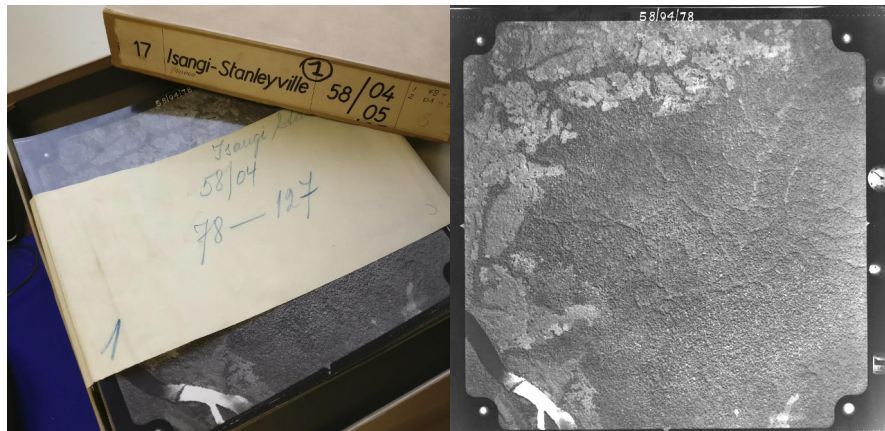


Figure 1. A box of historical aerial photographs (left) and a single aerial photograph (right) showing part of the Congo river. Note the meta-data provided in the right side margin of the image, such as acquisition time and flight height.

85 it. Thereafter, we selected flight paths 1 through 11 for digitization. From this larger dataset of 334
 86 images we selected 74 survey images for orthomosaic compositing and further analysis. All the
 87 selected images stem from the flight campaign made during January and February of 1958. The area
 88 includes the Yangambi village, 20 contemporary permanent sampling plots [30], past and present
 89 agricultural experimental plots [32] and large sections of the Yangambi **UNESCO Man and Biosphere**
 90 **reserve** surrounding to the west and east of the village. Although not formally mosaicked we provided
 91 a full dataset of pre-processed images using the cropping and normalization routines described below.
 92 The latter data was not used in subsequent LULCC analysis, but has been archived and made available
 93 to the public separately (see code & data availability statement below).

94 2.3. Digitization and data processing

95 All selected images, covering the Yangambi area, were contact prints as original negatives of the
 96 prints were not available. Images were scanned at a resolution exceeding their original resolution
 97 (or grain) at the maximal physical resolution of an Epson A3 flatbed scanner (i.e. 2400 dpi or 160 MP
 98 per image) and saved as lossless tiff images. Data were normalized using contrast limited histogram
 99 equalization [33] with a window size of 32 and a clip limit of 1.5. Fiducial marks were used to rectify
 100 and downsample the images into square 7700x7700 pixel images (~1200 dpi, 81 MP). This resulted in a
 101 dataset with digital images at a resolution that remained above the visible grain of the photographs,
 102 whilst the reduced image size facilitated easier file handling and processing speed.

103 Data was processed into a georeferenced orthomosaic using a Structure-from-motion (SfM, Ullman
 104 [34]) approach implemented in **Agisoft Metashape** version 1.5.2 (Agisoft LLC, St. Petersburg, Russia).
 105 An orthomosaic corrects remote sensing data to represent a perfectly downward looking image, free
 106 from perspective distortions due to topography and camera tilt. Using the SfM technique features,

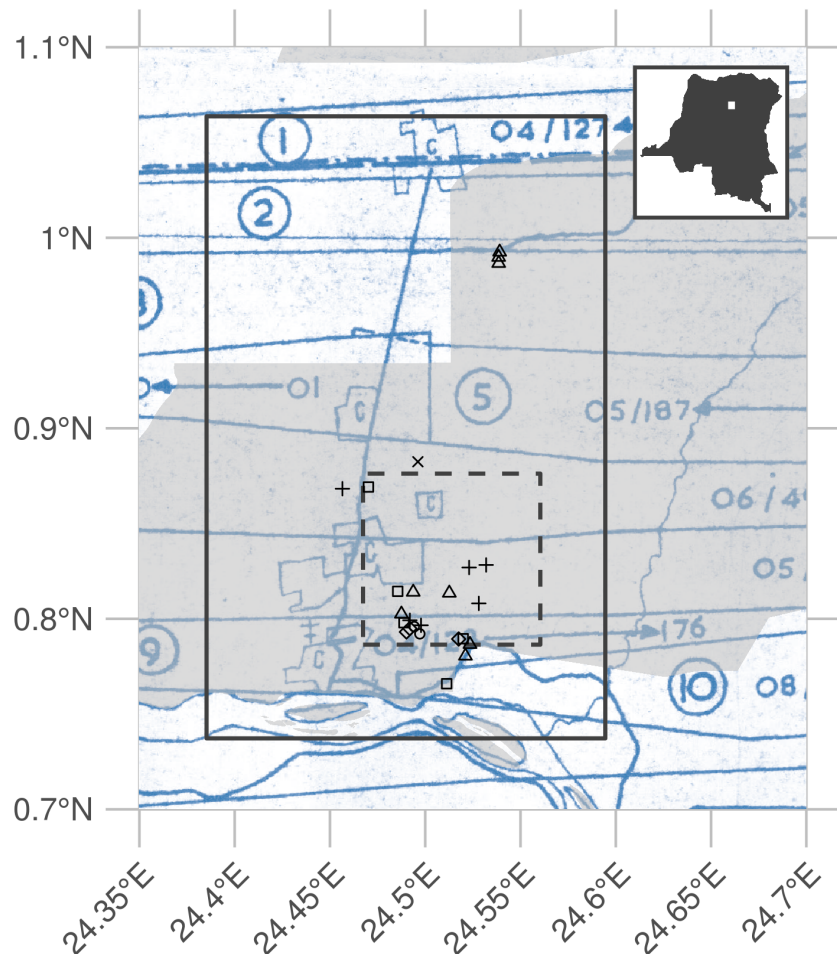


Figure 2. Overview of the historical flight paths during aerial photo acquisition and ancillary data used in this study. The bounding box of the orthomosaic data presented in this study is shown as a rectangle (23x36 km). The outline of a recent high-resolution Geo-eye panchromatic image is shown as a dashed dark grey rectangle (10x10 km). The location of various permanent sampling plots are shown as x, +, and open squares and triangles for the mixed, mono-dominant and edge plots respectively. The grey polygon delineates the current day Yangambi Man and Biosphere reserve. The inset, top right, situates the greater Yangambi region (white rectangle) with the DR Congo. The full flight plan and details are shown in Appendix Figure 1 and 2

107 areas in images with a large degree of similarity, are matched across various images to reconstruct
108 a three dimensional scene (topography) from two-dimensional image sequences. During the SfM
109 analysis we masked most clouds, glare or large water bodies such as the Congo river.

110 We calculated the orthomosaic using a low resolution point cloud and digital elevation map
111 (DEM). Additional ground control points were provided to assist in the referencing of image and
112 constrain the optimization routine used in the SfM algorithm. Ground control points consisted of
113 permanent structures which could be verified in both old and new aerial imagery (i.e. ESRI World
114 Imagery) and consisted of corner points of build structures (e.g. a building, bridge or swimming pool
115 etc.). Although most clouds were removed during the SfM routine some were retained to provide
116 sufficient SfM tie points to maximize continuous forest coverage in the final orthomosaic. The final
117 scene was cropped, to provide consistent wall-to-wall coverage of the reconstructed scene. The
118 orthomosaic was exported as a geotiff for further georeferencing in QGIS [35] using the georeferencer
119 plugin (version 3.1.9) and additional ESRI World Imagery high resolution reference data. We used 3rd
120 degree polynomial and 16 ground control points to correct the final image. Ground control points, raw
121 image data and final processed image are provided in addition to measures of uncertainty such as
122 mean and median error across all ground control points. All subsequent analysis are executed on the
123 final geo-referenced orthomosaic or subsets of it.

124 *2.4. Land-Use and Land-Cover Change*

125 *2.4.1. Classifying Land-Use and Land-Cover*

126 *Model training*

127 We automatically delineated all natural forest in the historical data, thus excluding tree plantations,
128 thinned or deteriorated forest stands which showed visible canopy cover loss, fields and buildings.
129 We used the Unet Convolutional Neural Net (CNN, Ronneberger *et al.* [36]) architecture implemented
130 in Keras [37] with an efficientnetb3 pre-processing backbone [38] running on TensorFlow [39] to train
131 a binary classifier (i.e. forest or non-forested). Training data were collected from the orthomosaic by
132 randomly selecting 513 pixel square tiles from locations within homogeneous forested or non-forested
133 polygons in the historical orthomosaic (Figure 5). Separate polygons were selected for training,
134 testing and validation purposes. Validation polygons were sampled 300 times, while both testing and
135 validation polygons were sampled at 100 random locations. Tiles extracted from locations close to the
136 polygon border at times contained mixed cover types. Tiles with mixed cover types were removed
137 from the list of source tiles (Table 1). Homogeneous source tiles were combined in synthetic landscapes
138 using a random gaussian field based binary mask (Figure 3). We generated 5000 synthetic landscapes

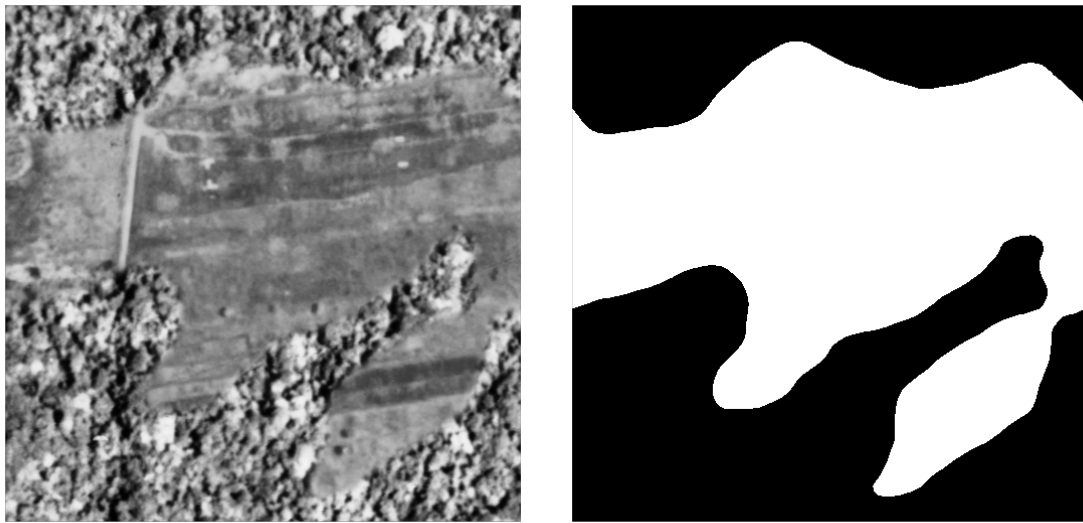


Figure 3. An example synthetic landscape, combining homogeneous forest and non-forest images into a patchy landscape using random gaussian field based masks. The left panel shows a combined synthetic landscape, while the right panel shows the corresponding forest (black) and non-forest (white) labels.

139 (balancing forest and non-forest classes) for training, while 500 landscapes were generated for both
 140 the validation and the testing datasets for a total of 6000 synthetic landscapes. In order to limit stitch
 141 line misclassifications, along the seams of mosaicked images, we created synthetic landscapes with
 142 different forest tiles to mimick forest texture transitions. We applied this technique to 10% of the
 143 generated synthetic landscapes (across training, validation and testing data).

Table 1. Number of source tiles used for the generation of synthetic landscapes.

	training	testing	validation
forest	300	100	100
non-forest	294	92	84

144 The CNN model was trained for 100 epochs with a batch size of 30 using Adam optimization [40],
 145 maximizing the Intersect-over-Union (IoU) using Sørensen–Dice [41] and categorical cross-entropy
 146 loss functions. Data augmentation included random cropping to 320 pixel squares, random orientation,
 147 scaling, perspective, contrast and brightness shifts and image blurring. The optimized model was used
 148 to classify the complete orthomosaic using a moving window approach with a step size of 110 pixels
 149 and a majority vote (> 50% agreement) across overlapping areas to limit segmentation edge effects.
 150 In addition, we provide raw pixel level classification agreement data for quality control purposes
 151 (see Data availability below). We refer to Figure 4 for a synoptic overview of the full deep learning
 152 workflow.

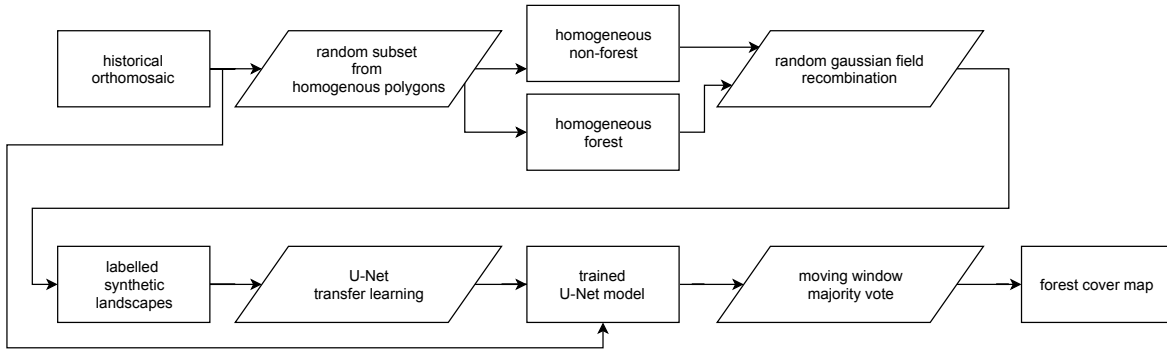


Figure 4. A diagram of the deep learning workflow followed in training a binary forest / non-forest cover convolutional neural net U-Net model to generate our forest cover map.

153 *Model validation*

154 We report the CNN accuracy based upon the IoU of our out-of-sample validation dataset of
155 synthetic landscapes. In addition, we report confusion matrices for all pixels across the homogeneous
156 validation polygons, as well as the training and testing polygons (see Figure 5). Furthermore, we used
157 the first acquisition of a recent pan-chromatic Geo-Eye 1 stereo pair (Geo-Eye, Thornton, Colorado,
158 U.S.A., order 737537, 2011-11-11 08:55 GMT or 09:55 local time) to classify and assess the robustness
159 of the CNN algorithm on contemporary remote sensing imagery with similar spectral and spatial
160 characteristics. We used the Global Forest Change version 1.6 (GFC, tile 10N-020E) [1] map data,
161 capturing deforestation up to 2011, to quantify accuracy on downsampled CNN Geo-Eye classification
162 results. Once more, we report the confusion matrix between the GFC and CNN derived forest cover
163 maps, masking clouds and cloud shadows. To summarize confusion matrices we report accuracy as:

$$\text{Accuracy} = \frac{(TP+TN)}{(TP+TN+FP+FN)}$$

164 in which TP, TN, FP, FN are True Positive, True Negative, False Positive and False Negative,
165 respectively.

167 **2.4.2. Characterizing long term change**

168 To map long term LULCC in the Yangambi region we used the contemporary Global Forest
169 Change version 1.6 (GFC, tile 10N-020E) (lossyear) map data [1]. Using the GFC data we calculated the
170 latest state of the forest with respect to the conditions at the start of 1958, 60 years earlier. In our analysis
171 we only included GFC pixels which recorded no forest loss throughout the whole 2000 - 2018 period.
172 Forest loss in the context of GFC is defined as “a stand-replacement disturbance, or a change from a
173 forest to non-forest state”. As such, locations which would see reforestation or deforestation between
174 2000 and 2018 would be marked as non-forest (i.e. disturbed). As the resolution of the historical forest
175 classification exceeds that of the GFC map we downsampled our historical forest cover data to 30
176 m GFC resolution using a nearest neighbour approach. We masked out all water bodies using the

177 Global Forest Change survey data mask layer, and limited the analysis to the right bank of the Congo
178 river. We provide summary statistics of historical and contemporary deforestation and reforestation.
179 We map permanent deforestation after 1958, reforestation after 1958, recent deforestation and long
180 term (stable) forest cover. All references to changes over time in the context of our analysis explicitly
181 compare the historical and contemporary periods from hereon forth.

182 2.4.3. Landscape fragmentation & Above Ground Carbon estimates

183 To quantify changes in the structure of forest cover and its disturbances we used spatial landscape
184 pattern analysis (i.e. fragmentation) metrics [42]. Landscape metrics provide a mathematical framework
185 for the analysis of discrete land-cover classes and allows us to capture their composition and
186 configuration. These metrics are therefore commonly used to compare how landscapes change over
187 time [43]. In particular, fractals provide a way to quantify complex natural landscapes, including their
188 self-similarity across scales [44,45]. We report the ratio of edge to area and the fractal dimension to
189 quantify landscape complexity of forest disturbances. A fractal dimension closer to 2 suggest a more
190 complex (fragmented) landscape.

191 Statistics were calculated for all forest disturbance patches larger than 1 ha and smaller than the
192 95th percentile of the patch size distribution using the R package “landscapemetrics” [43]. We provide
193 mean and standard deviation on edge, area, their ratio and fractal dimension for both the historical
194 and contemporary Hansen *et al.* [1] forest cover maps.

195 We estimated above ground carbon (AGC) losses and gains, due to deforestation and reforestation,
196 using plot based averages of recent inventory data at permanent sampling plots in the area (Figure 2).
197 We refer to Kearsley *et al.* [30] for the survey method and allometric relations used to scale the survey
198 data. Unlike standard square 1 ha plots, edge plots ($163.03 \pm 19.39 \text{ Mg C ha}^{-1}$, N = 5) were set back
199 200 m from forest edges and were 50x200 m, with the 50 m side of the plot along the forest edge and
200 continuing 200 m into the forest (Appendix Table 2). We further confirmed that forest edge plots, as
201 compared to mixed forest plots ($160.48 \pm 23.84 \text{ Mg C ha}^{-1}$, N = 8, see Appendix Table 3 for all forest
202 types), did not show a significantly different AGC (Mann Whitney U test, p < 0.05). Thus it was not
203 necessary to explicitly quantify changes in AGC caused by edge effects. Moreover, we used the mean
204 value, and its uncertainty (i.e. standard deviation), of the mixed forest as representative for potential
205 AGC losses. Despite the challenges inherent in quantifying AGC for forest edges we mapped the total
206 extent of the edges in the contemporary landscape. To align our landscape analysis with exploratory
207 analysis of the survey data we used a buffer of 200 m to estimate the extent of forest edges and patches,
208 up to the location of forest edge plots.

Surveys of old plantations show a large variation in AGC, depending on age and the crop type. For example, the AGC values varied from 86.55 to 168.67 Mg C ha⁻¹, for *Elaeis guineensis* (oil palm) and *Hevea brasiliensis* (rubber tree) plots respectively (Bustillo *et al.* [46], personal communications). These higher values are in line with the mixed plot AGC estimates (160.48 ± 23.84 Mg C ha⁻¹, N = 8) in the area, while the palm plantations resemble old-regrowth values (81.87 Mg C ha⁻¹, N = 1). To quantify AGC in reforested areas we therefore use both AGC estimates of old-regrowth and mixed forest, as lower and upper bounds. We did not have sufficient data to account for individual changes in AGC across plantations.

2.5. Canopy structure & FOTO texture analysis

We compared the structure of the canopy both visually and using Fourier Transform Textural Ordination (FOTO, Couturon [47]). FOTO uses a principal component analysis (PCA) on radially averaged 2D Fourier spectra to characterize canopy (image) texture. The FOTO technique was first described by Couturon [47] to quantify canopy stucture in relation to biomass and biodiversity, and can be used across multiple scenes using normalization [16].

We used the standard FOTO methodology with fixed zones, instead of the moving window approach. The window size was set to the same size (187 pixels or ~150 m) as used in the moving window analysis above. To account for illumination differences between the two scenes we applied histogram matching. No global normalization was applied, as the scene was processed as a whole. PC values from this analysis for all permanent sampling plots in both image scences were extracted using a buffer with a radius of 50 m.

For both site based and scene analysis we correlated PC values with permanent sample plot inventory data such as stem density, above ground biomass and tree species richness (Appendix Table 2-3). Additional comparisons are made between contemporary Geo-Eye data and the historical orthomosaic derived PC values. Due to the few available permanent sampling plots in both scenes we used a non-parametric paired signed rank (Wilcoxon) test [48] to determine differences between the PC values of the Geo-Eye and historical orthomosaic image scenes across mono-dominant and mixed forest types. In all analysis, mono-dominant site 4 was removed from the analysis due to cloud contamination.

3. Results

3.1. Orthomosaic construction

Our analysis provides a first spatially explicity historical composite of aerial survey images in support of mapping land-use and land-cover within the Congo Basin. The use of high resolution

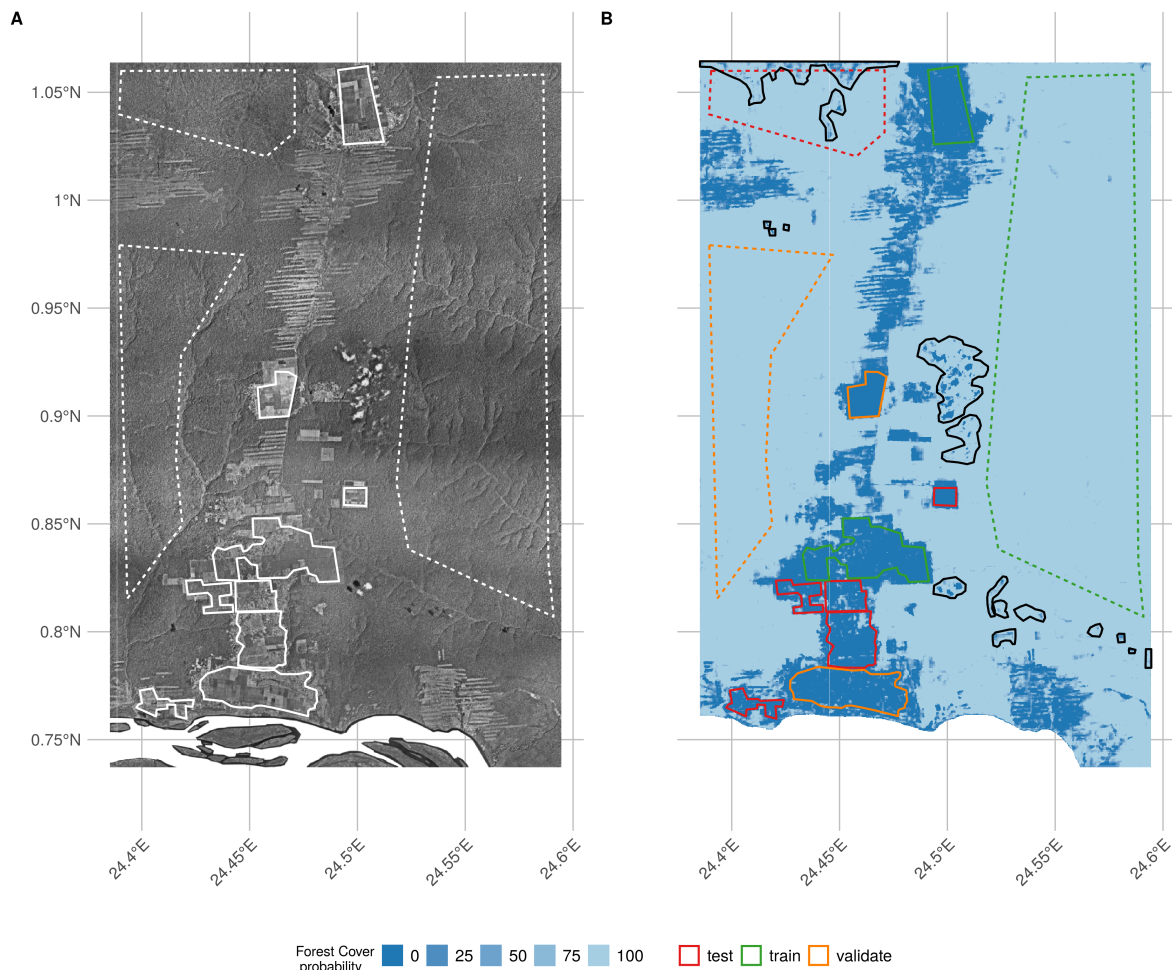


Figure 5. Overview of the final orthomosaic of the greater Yangambi region (A) as well as the forest cover classification uncertainty (B) used to generate the final Land Cover map (see Figure 6). Homogeneous polygons used in the generation of the synthetic landscape for Convolutional Neural Network training, testing and validation are marked as dashed and full lines for forest and non-forest regions, respectively. Training, testing and validation regions are denoted in panel B in green, red and orange, respectively. Black polygon outlines denote cloud and image stitch line regions which were manually excluded from analysis, but retained in calculation of validation statistics (see Table 2).

historical images combined with SfM image processing techniques allowed us to mosaic old imagery across a large extent. The final orthomosaic composition of the Yangambi region provided an image scene covering approximately 733 million pixels across ~93 431 ha with a resolution of 0.88 m / pixel (or ~23x36 km, Figure 2). The overall spatial accuracy of the SfM orthomosaic composition using the sparse cloud DEM (with a resolution of 45.8 m/pixel) was limited to approximately 23 m. Further georeferencing outside the SfM workflow reduced the mean error at the ground control points to 5.3 ± 4.9 px (~ 4.7 ± 4.3 m), with a median error of 2.9 px (2.6 m). The orthomosaic served as input for all subsequent LULCC analysis with all derived maps provided with the manuscript repository (see data & code availability statements below).

250 *3.2. Land-use and Land-Cover Classification*

251 *3.2.1. CNN model validation*

252 The CNN deep learning classifier reached an Intersection-over-Union accuracy of 97% on the
253 detection of disturbed forest in the out-of-sample (validation) synthetic landscape data. Using all pixels
254 within the validation polygons (Figure 5) showed a similar accuracy value of ~98%. Using all polygons
255 across the scene, including those used in the generation of testing and training synthetic landscapes,
256 increased the accuracy to ~99% (Table 2). A comparison with recent pan-chromatic Geo-Eye data
257 shows good agreement, with an accuracy of ~87% across all pixels, between the landsat based GFC
258 data and downscaled CNN results (Table 2 and Figure 7).

Table 2. Confusion matrix showing % agreement between forest / non-forest classes using a Convolutional Neural Network (CNN) across previously selected homogenous areas. In addition, overall accuracy is reported for each confusion matrix.

CNN	Geo-Eye (full scene)		Aerial Survey (all polygons)		Aerial Survey (validation polygons)	
	non-forest	forest	non-forest	forest	non-forest	forest
non-forest	10.17	8.55	97.4	0.19	98.59	0.0
forest	3.75	77.52	2.6	99.81	1.41	100.0
Accuracy	87.70			98.61		99.3

259 *3.3. Long term changes in LULC and Above Ground Carbon*

260 Scaling our classifier to the whole historical orthomosaic we detected ~16 200 ha (or ~20% of the
261 scene) of disturbed forests. A large fraction of the disturbed area was restored in the period between
262 the two acquisition periods. In total, 9918 ha, or little over half of the affected forest was restored
263 (Figure 5C-D, dark blue). Recent deforested areas, as registered through satellite remote sensing (>
264 2000), approximate 8776 ha (Table 3, Figure 6 - light green).

265 Recent deforestation follows a distinctly different pattern compared to historical patterns.
266 Historical deforestation showed a classical fishbone pattern for forest clearing with very sharp edges,
267 while current patterns are patchy and ad-hoc (figure 6C, dark blue and green colours respectively).
268 These differences are reflected in the analysis of landscape metrics of deforestation. Between the
269 historical and contemporary LULCC maps we see an increase in small disturbances, as indicated by
270 the decreasing area of the mean patch size, down to $\sim 1.86 \pm 0.75$ ha from $\sim 5.25 \pm 5.02$ ha historically.
271 Perimeter lengths were longer historically, at 1451 ± 943 m, compared to contemporary landscapes
272 $\sim 921 \pm 362$ m (Table 4). This shift in perimeter area ratio led to a similar change in the fractal index,
273 slightly increasing in value to 1.1 ± 0.05 from 1.09 ± 0.04 over time. Values closer to a fractal index of
274 2 suggest a more complex (fragmented) landscape.

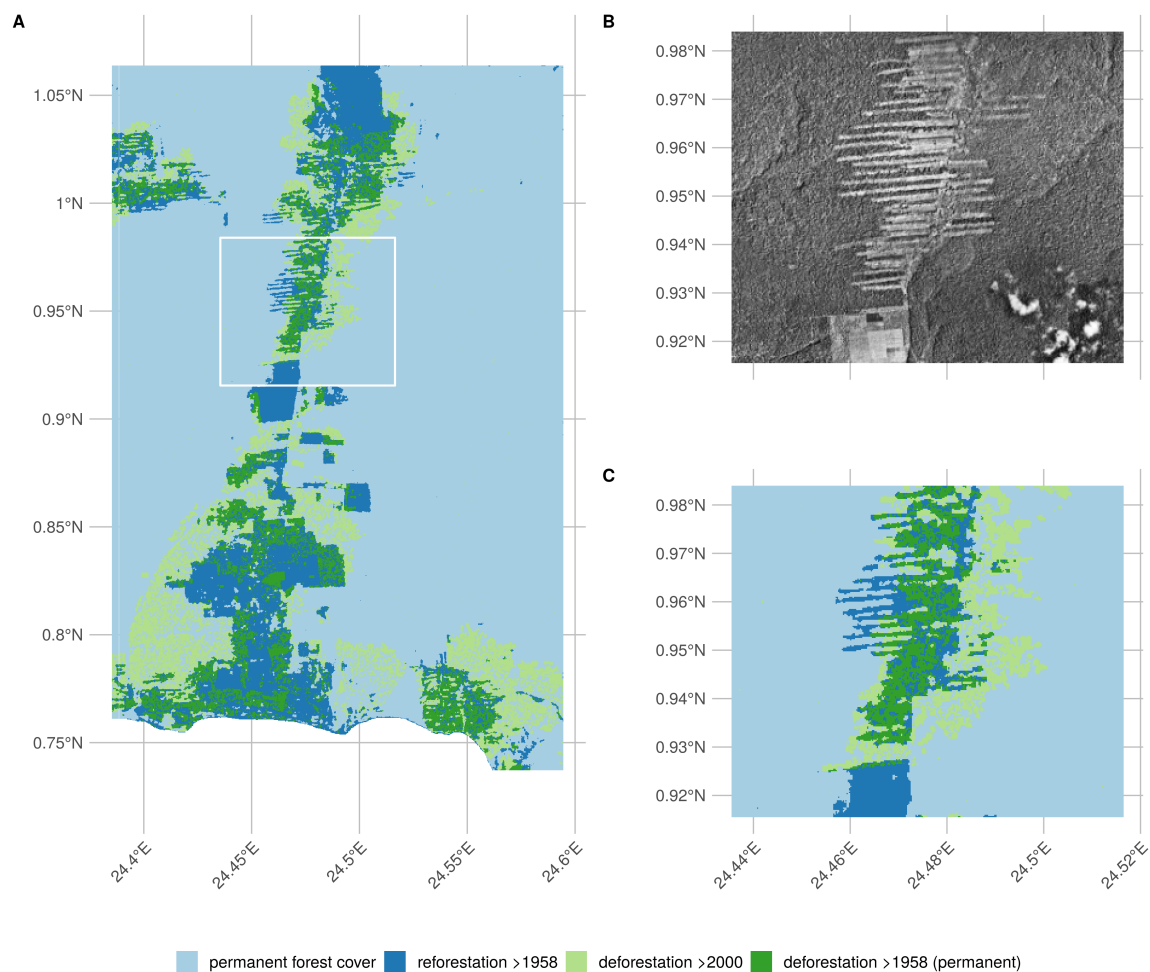


Figure 6. Overview of the final Land Use Land Cover Change map, a detailed inset of both the underlying orthomosaic (B) and the derived land use land cover change map displayed as the difference between the Convolutional Neural Network based classification orthomosaic and the recent Landsat based forest cover map by Hansen et al. 2013 (C).

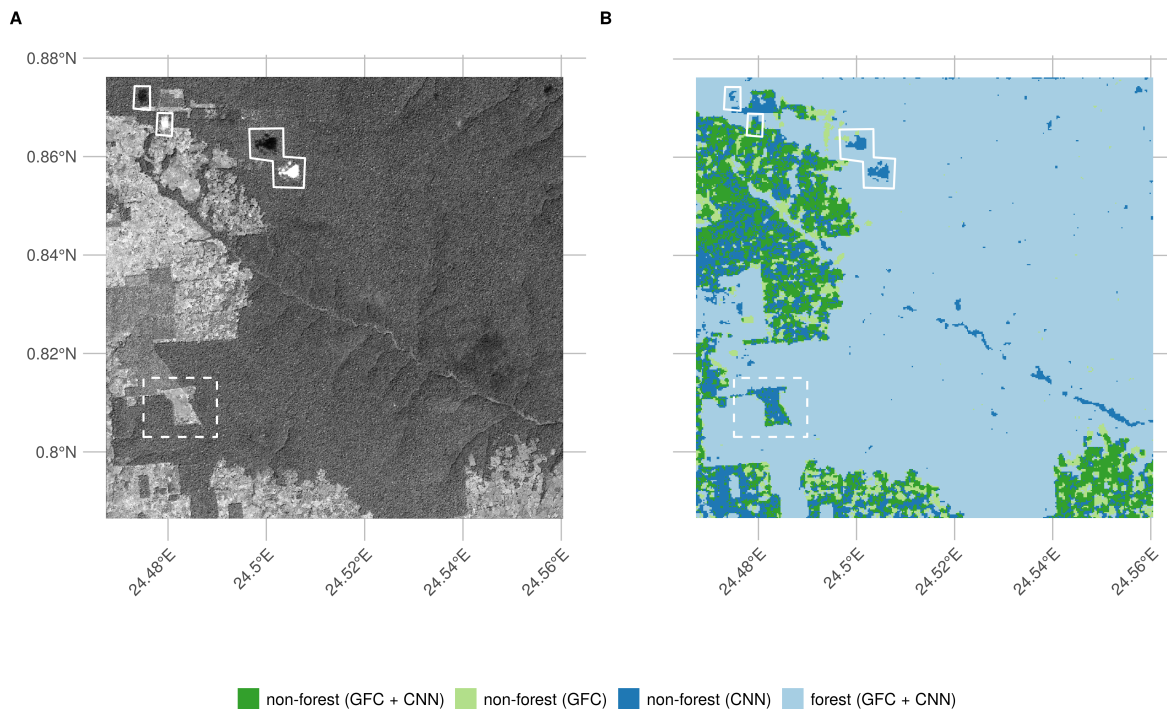


Figure 7. Convolutional Neural Network (CNN) based forest cover classification results (B) as run on a recent (2011) Geo-Eye panchromatic image (A). We show the difference between the Convolutional Neural Network based classification and a recent Landsat based forest cover map by Hansen et al. 2013. Full white outlines denote cloud contamination, the dashed rectangle shows a location where the CNN outperforms the Landsat based forest classification.

275 A comparison of forest edge plots with mixed forest plots showed no significant difference in
 276 AGC, or other reported values such as species richness, basal area or stem density (Mann Whitney U
 277 test, $p < 0.05$). Edge influence did not extend beyond 200 m from a forest edge, but still represented an
 278 area of 13 151 ha (Table 3).

279 Changes in both land-use and land-cover led to concomitant changes in AGC stocks. Recovery
 280 throughout the region was characterized for patches of forest and plantations. Assuming high density
 281 stands, based on previous work, this could amount to a carbon gains of up to 1592 Gg C across our
 282 study area, offsetting more recent losses of approximately 1408 ± 209 Gg C. On the other hand, at the
 283 low end, if we assume a lower carbon density of $81.8 \text{ Mg C ha}^{-1}$ this would result in a total carbon
 284 gain of 811 Gg C. Using our approach results indicate that overall deforestation around Yangambi has
 285 resulted in a loss of $\sim 2416 \pm 358$ Gg C in AGC stocks.

286 *3.4. Canopy structure & FOTO texture analysis*

287 Visual interpretation of the scenes provide evidence that most locations do not change dramatically
 288 with respect to canopy composition, except for the large areas of disturbances in contemporary fallow
 289 or young-regrowth plots. One marked difference is noted in the mono-dominant plot 6 (Appendix
 290 Table 2). Here, the current mono-dominant *Brachystegia laurentii* is a recent development, changing the

Table 3. Land use land cover change statistics of forest cover around Yangambi in the central Congo Basin. The data evaluates a difference between a historical (1958) aerial photography based survey and the Hansen et al. 2013 based satellite remote sensing data. Spatial coverage statistics are provided hectares (ha), rounded to the nearest integer as well as Above Ground Carbon (AGC) scaled using recent survey measurements.

	AGC	
	ha	Gg C
Total scene area	93431	
Non-forest cover (1958)	16200	
Forest cover	68455	
- of which forest edges	13151	
reforestation >1958	9918	811 - 1592
deforestation >2000	8776	1408 ± 209
deforestation >1958 (permanent)	6282	1008 ± 150

Table 4. Landscape metrics for historical and contemporary deforestation patterns. We report patch perimeter and area, their ratio and fractal dimension. Values are reported as mean ± standard deviation, across all deforestation patches.

	perimeter (m)	area (ha)	ratio (m^{-1})	fractal dimension
historical	1451.58 ± 943.27	5.25 ± 5.02	0.03 ± 0.01	1.09 ± 0.04
contemporary	921.74 ± 362.59	1.86 ± 0.75	0.05 ± 0.01	1.1 ± 0.05

canopy structure visibly during the last half century (Figure 8). The previous varied canopy structure gave way to a more dense and uniform canopy. This is reflected in a change of the FOTO PC value from 0.19 historically to its current value of 0.54 (Figure 9). This historical value is similar to the mean of contemporary mono-dominant stands of *Gilbertiodendron dewevrei* with PC averaging 0.34 ± 0.1 , and is only slightly higher than historical values for a mixed forest (0.18 ± 0.08 , Figure 9). The reverse pattern is seen in the contemporary PC values. Here, the value of 0.54 exceeds those of most mono-dominant stands (0.35 ± 0.08), and is even further removed from the values noted for mixed forests (0.12 ± 0.03 , Figure 9).

Using only small subsets around existing permanent sampling plots we show distinct differences between forest types, with PC values in both historical and contemporary imagery markedly higher for the mono-dominant forest types compared to all others (Appendix Figure 4). Provided that the young-regrowth and fallow permanent sampling plots have seen recent disturbance the Wilcoxon signed rank test on the mixed and mono-dominant plots between the historical and contemporary PC values did not show a significant difference ($p > 0.05$). Similarly, no significant different using PC values extracted from the whole scene analysis was noted ($p > 0.05$). Any relationships between contemporary Geo-Eye data and permanent sampling plot measurements of Above Ground Carbon, stem density and species richness were non-significant ($p > 0.05$, Appendix Figures 4-6).

Furthermore, visual inspection of the scene wide analysis suggests historical scences do not show landscape wide canopy features (Figure 10 A-B), unlike the contemporary scene (Figure 10 C-D). In the

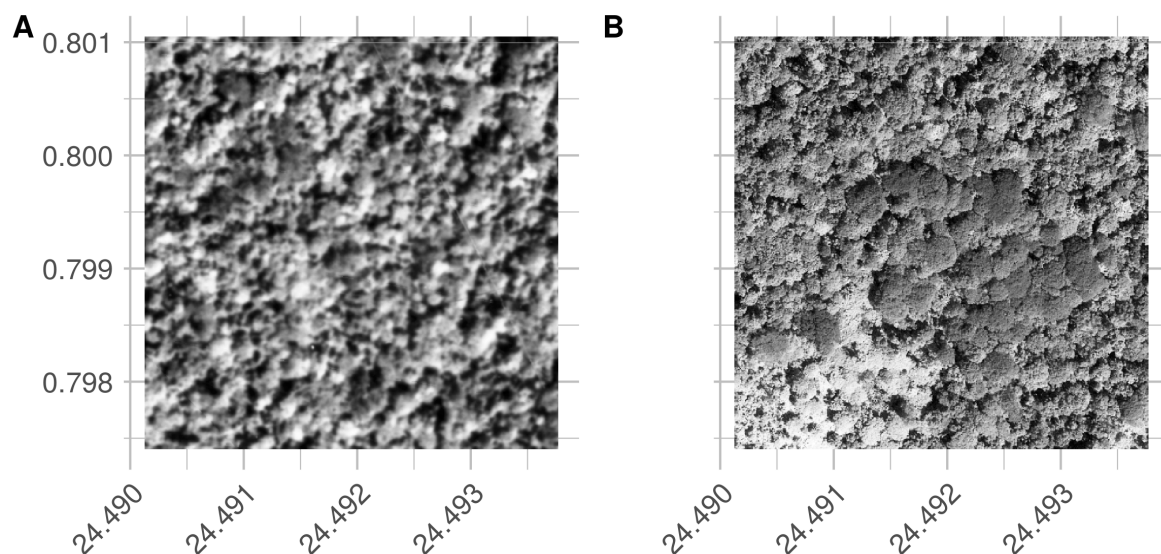


Figure 8. Visual comparison between a historical (A) and contemporary (B) permanent sampling plot. The site is currently listed as a mono-dominant *Brachystegia laurentii* stand. Note the structural differences with a 'coarse' canopy structure in the historical image compared to the more closed contemporary stand.

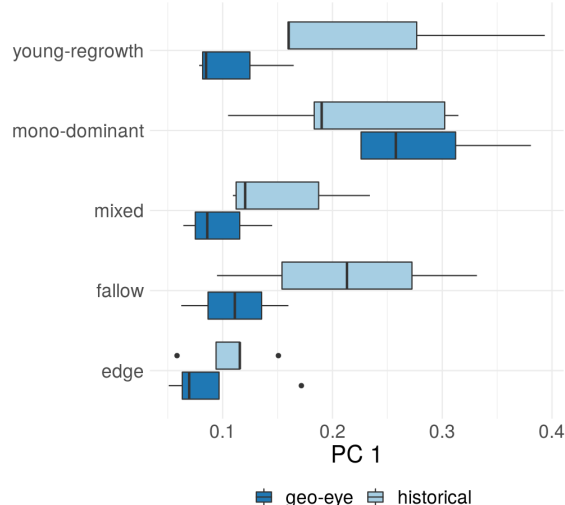


Figure 9. Boxplots comparing the first principal component (PC1) of a site based FOTO analysis across different forest types for both contemporary (Geo-Eye) and historical orthomosaic data.

310 contemporary scene the FOTO algorithm picks up landscape features such as changes in texture along
311 the river valley (the diagonal line in Figure 10D). However, no corresponding landscape patterns are
312 found by the FOTO algorithm in the historical orthomosaic.

313 4. Discussion

314 Finely grained spatial data sources, such as remote sensing imagery, are rare before the satellite era
315 (<1972). This lack of data limits our understanding of how forest structure has varied over longer time
316 periods in remote areas. Long term assessment can be extended by using large inventories of historical
317 aerial survey data [22,23,49]. Despite the difficulties in recovering this data and its limitations, such
318 as invisible disturbances [50], remote sensing generally remains the best way to map and quantify
319 LULCC [2]. In our study we used novel numerical remote sensing techniques to valorize, for the
320 first time, historical remote sensing data in order to quantify (long term) land-use and land-cover
321 change and canopy structural properties in the central Congo Basin. Despite these successes some
322 methodological and research considerations remain.

323 4.1. Methodological considerations

324 4.1.1. Data recovery challenges

325 In our study the archive data recovered was limited to contact prints and therefore did not
326 represent the true resolution of the original negative. In addition, analogue photography clearly
327 produces a distinct softness compared to digital imagery (Figure 8). Despite favourable nadir image
328 acquisitions [51] image softness combined with illumination effects between flight paths, and the
329 self-similar nature of vast canopy expanses [52–54], limited our ability to provide wall-to-wall
330 coverage of the entire dataset containing 334 images. Few man made features in the scenes also
331 made georeferencing challenging. Although the village of Yangambi provided a range of buildings
332 as (hard-edge) references other areas within the central Congo Basin might have fewer permanent
333 structures and would require the use of soft-edged landscape features (e.g. trees, river outflows).
334 Research has shown that soft-edged features can help georeference scenes even when containing few
335 man-made features [55]. Our two step georeferencing approach resulted in a referencing accuracy of
336 ~4.7 ± 4.3 m across reference points. However, it should be noted that referencing accuracy of the final
337 scene is less constrained toward the edges of the scene.

338 4.1.2. LULC classification & validation

339 When classifying the orthomosaic into forest and non-forest states we favoured a deep learning
340 supervised classification using a CNN over manual segmentation to guarantee an “apples-to-apples”

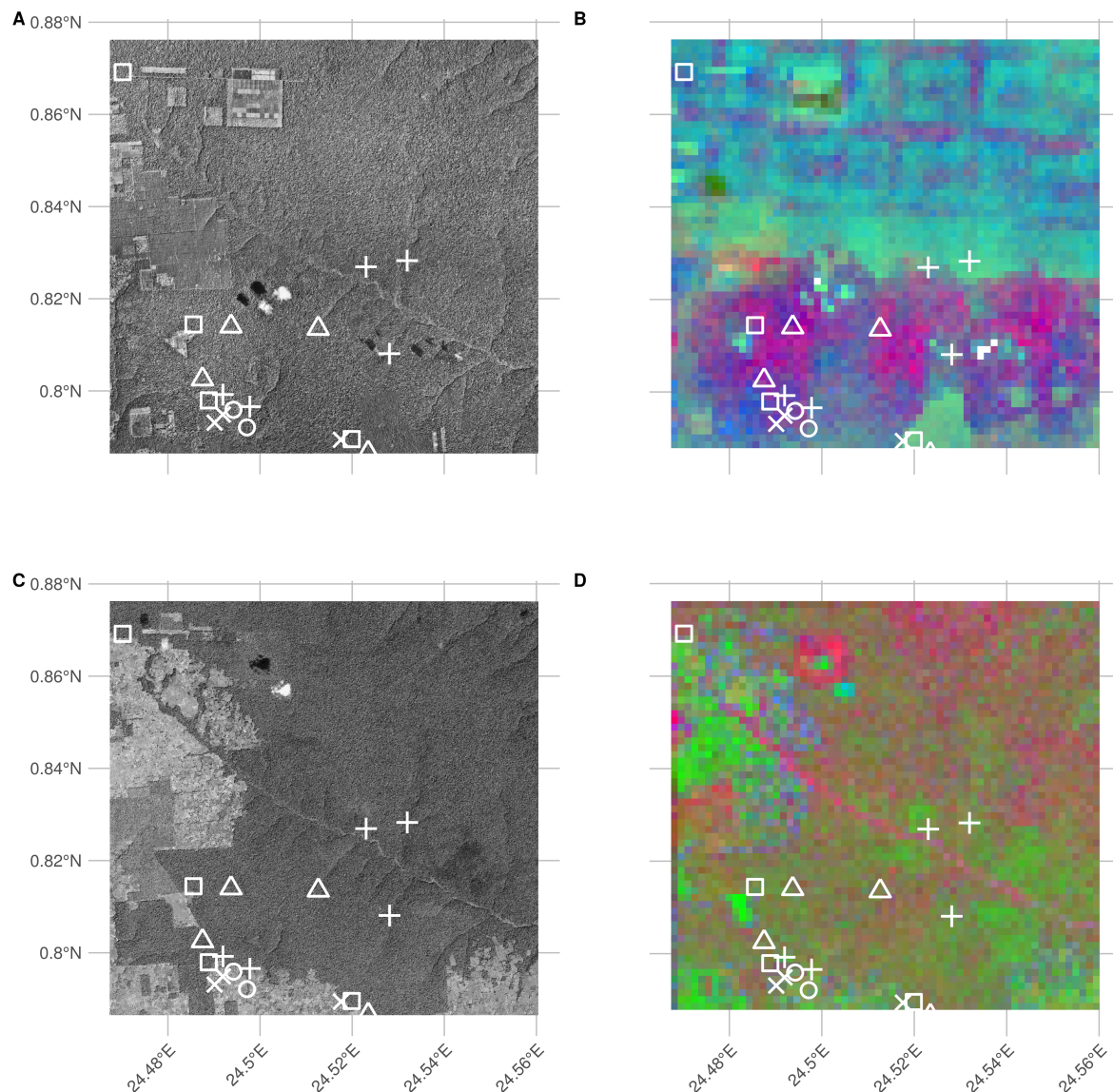


Figure 10. RGB visualizations of the first three principal components of scene wide FOTO texture analysis of historical and current (Geo-Eye) imagery. Current permanent sampling plots of mono-dominant, mixed, fallow and young (edge) forest plots are marked with open triangles, open circles, open squares and crosses, respectively.

341 comparison between the historical and the contemporary GFC forest cover map used in our analysis.
342 We acknowledge that both the CNN and GFC land-use and land-cover maps use different underlying
343 features, i.e. spatial or spectral data, yet attain a similarly high accuracy of up to 99% [1]. More so,
344 when validating our CNN classifier against GFC data (Figure 7) for a contemporary high resolution
345 Geo-Eye panchromatic image we reach an accuracy of ~87%, despite a time difference of almost 60
346 years. Visual inspection of the classification data in Figure 7 suggests that the GFC map more often
347 than not classifies non-forest areas as forest. Actual classification accuracy of our algorithm might
348 therefore be higher than our reported value.

349 4.1.3. Scaling opportunities

350 Our approach uses broadly defined homogeneous polygons to construct a balanced dataset of
351 synthethic landscapes. The methodology is analoguous to the use of sparse labelling as used by
352 Buscombe and Ritchie [56] and contrasts with the standard methodologies which generally extract
353 pixel (windows) [22] or delineate land cover classes [23] to drive a classifier or analysis. More so, the
354 use of heavy image augmentation during model training sidesteps texture representation issues which
355 affect classification of image scenes with inconsistent illumination or sharpness [25] or ad-hoc feature
356 engineering [22]. The use of synthetic landscapes allowed us to account for most, but not all, of the
357 variability within our orthomosaic. Our analysis has shown that despite being trained on historical
358 data our model could map contemporary forest cover in remote sensing data with similar spatial and
359 spectral characteristics (Figure 7), suggesting that the classifier consistently works across both space
360 and time. We acknowledge that the use of synthetic landscapes is limited by the available homogeneous
361 areas to sample from and the number of classes. Yet, the latter should not be a constrained as previous
362 research efforts have focussed on simple forest cover maps [1].

363 4.2. Research context

364 4.2.1. Long term changes in LULC and Above Ground Carbon

365 Our analysis shows that the majority of deforestation around Yangambi happened toward the late
366 1950s (~16 200 ha). Considerable reforestation has occurred since the aerial survey was executed (~9918
367 ha), and socio-economic instability prevented further large scale forest exploitation. In particular, many
368 plantations have reached maturity and forest has re-established in previously cleared or disturbed
369 areas. The majority of this reforestation takes the form of isolated patches of forest but is offset
370 by further deforestation of previously untouched forest. Generally, the function and structure of
371 forests can be influenced by forest edges that are located up to 1 km away however most effects are
372 pronounced within the first 300 m from the edge [57]. Our analysis of edge effects on AGC has shown

that the influence is negligible 200 m away from the edge. Phillips *et al.* [58] have shown similar weak responses to edge effects in the Amazon forest. Due to a lack of data on the extent (depth) of edge effects and their influence on AGC beyond 200 m we did not include any estimates of carbon loss or gain within these zones. However, it must be stated that edges throughout the landscape make up a substantial area and account for 13 151 ha. Thus edges could have a substantial negative [6] or positive [59] influence on AGC. Similarly, uncertainties in how to explicitly correct for plantations in the landscape present a further challenge. Similarly, variability across mixed forest plots used in scaling above ground carbon estimates due to deforestation introduced additional uncertainty (see Appendix Table 3). Thus, although our estimates are only indicative they do underscore the important influence of landscape structure in carbon accounting. However, our findings do not indicate that deforestation in Congo basin is declining, on the contrary.

Over the past half century there has been a clear shift in land use in Yangambi (Figure 5). Land use has shifted away from a regular (fishbone) deforestation pattern that emerges when (large scale) agricultural interests dominate the landscape [60], to a more fragmented landscape (Figure 5D). The former is consistent with historical land management at the time of the aerial survey [46]. These regular patterns reversed due to a decrease in large scale intensive agriculture and an increase in ad-hoc small scale subsistence farming with large perimeter to area relationships (i.e. ragged edges). Consequently, edge effects in the current landscape are far more pronounced than in the historical scene.

Visual inspection of the images also suggests that reforestation within the historically cleared areas and experimental plots is not necessarily limited to areas far removed from more densely populated areas. For example, large reforested areas exist close to the Congo stream and Yangambi village itself (Fig. 5). Here, regional political components, such as land leases and large scale ownership could have played a role in safeguarding some of these areas for rewilling or sustainable management [61,62]. Despite widespread anthropogenic influences throughout the tropics [31] the retention of these forested areas show the potential of explicit or implicit protective policy measures (e.g. INERA concessions, Bustillo *et al.* [46]) on a multi-decadal time scale. Reforestation in non-continuous areas within Yangambi could increase landscape connectivity and help increase biodiversity [12].

Our analysis therefore provides an opportunity to highlight and study those regions that have previously suffered confirmed long-term disturbances, and those that have been restored since. Assessments of old plantations and recovering clear-cut forests can serve as a guide to help estimate carbon storage capacity and forest recovery rates in managed and unmanaged conditions [18,20,63] over the mid- to long-term, in support of rewilling and general forest restoration [12,61,62]. In addition, mapping long-term edge effects can further support research into issues such as receding forest edges [57].

407 4.2.2. Canopy structure & FOTO texture analysis

408 Finally, the FOTO technique used to quantify relationships between canopy structure and forest
409 characteristics rendered no valuable insights of either the historical orthomosaic or recent Geo-Eye
410 scene. Similarly weak correlations were found previously by Solórzano *et al.* [64]. In contrast, site
411 based texture metric statistics did show correspondence between historical and contemporary satellite
412 imagery. None of them were either consistent or significant. Although visual interpretation shows
413 distinctly different canopy structures (Figure 5) the differences in how resolution is defined and issues
414 related to image quality prevented us from quantifying these further. Unlike large scale studies by
415 Ploton *et al.* [14] we could not scale this technique to historical data. The successful use of our CNN
416 classification model on a contemporary remote sensing data does suggest that texture can be used
417 to consistently capture canopy properties 60 years apart. Differences in PC between forest types
418 (e.g. mono-dominant vs. mixed, Figure 9) corroborate that texture can serve as a basis for LULC
419 classification. However, inflexibility on part of the FOTO technique in dealing with non-standardized
420 (historical) data, or scaling these results to AGC values, limits its use case. We advise that future
421 valorisation efforts should preferentially work from foto negatives (if available) to ensure optimal data
422 quality in resolution, contrast and sharpness.

423 5. Conclusion

424 Given the impact of tropical forest disturbances on atmospheric carbon emissions, biodiversity
425 and ecosystem productivity accurate long term reporting of LULCC is an imperative. Our analysis of
426 historical aerial survey images (1958) of the Central Congo Basin provides a window into the state of
427 the forest at the start of the anthropocene. The use of a CNN based LULC classifier, using synthetic
428 landscapes based image augmentation, provides a robust semi-supervised solution which scales across
429 space and time, even for image scenes with inconsistent illumination or sharpness. Combined with
430 contemporary remote sensing data we have shown that historical aerial survey data can be used to
431 quantify long-term changes in LULC and AGC. We showed a shift from previously highly structured
432 industrial deforestation of large areas for plantation purposes, to discrete smallholder clearing for
433 farming, increasing landscape fragmentation but also opportunities for substantial regrowth. Efforts to
434 quantify canopy texture features and their link to AGC had limited to no success. Our analysis provides
435 insights into the rate at which deforestation and reforestation has taken place over a multi-decadal
436 scale in the central Congo basin. As such, it provides a useful historical context while interpreting past
437 and ongoing forest research in the area.

438 6. Additional Information and Declarations**439 6.1. Data availability**

440 Hufkens et al. (2019). A curated dataset of aerial survey images over the central Congo Basin, 1958.
441 Zenodo: <https://doi.org/10.5281/zenodo.3547767>. All data not included in the latter repository can be
442 found bundled with the analysis code as listed below. Proprietary datasets (i.e. Geo-Eye data) are not
443 shared, but purchase order numbers allow for acquisition of these datasets to ensure reproducibility.

444 6.2. Code availability

445 All analysis code is available as an R / python [65] projects (<https://khufkens.github.io/orthodrc>
446 & https://khufkens.github.io/orthodrc_cnn/). The analysis relied heavily on the ‘raster’ [66],
447 ‘RStoolbox’ [67], and ‘landscapemetrics’ [43] packages, while post-processing and plotting was
448 facilitated by the ‘tidyverse’ ecosystem [68], ‘ggthemes’ [69], ‘scales’ [70] and ‘cowplot’ [71]. Additional
449 plotting elements were formatted or provided by ‘sf’ [72] and ‘rnatural-earth’ [73] packages, respectively.
450 I’m grateful for the contributions to the scientific community by the developers of these packages.

451 **Acknowledgments:** This research was supported through the Belgian Science Policy office COBECORE project
452 (BELSPO; grant BR/175/A3/COBECORE). K.H. acknowledges funding from the European Union Marie
453 Skłodowska-Curie Action (project number 797668). K.H. grateful for the support of T.d.H. volunteering his
454 time in scanning the images.

455 **Author Contributions:** K.H. conceived and designed the study, analyzed the data, prepared figures, tables and
456 authored the final draft of the manuscript. T.d.H. scanned all image data. E.K. and T.d.H. provided plot based
457 AGC estimates. T.D., K.J., E.K, H.B., P.S., F.V.S.M., M.A., J.V.D.B., H.V and L.W. reviewed the final manuscript.

458 **Conflicts of Interest:** The authors declare no conflict of interest. The founding sponsors had no role in the design
459 of the study; in the collection, analyses, or interpretation of data; in the writing of the manuscript, an in the
460 decision to publish the results.

461 References

- 462 1. Hansen, M.C.; Potapov, P.V.; Moore, R.; Hancher, M.; Turubanova, S.A.; Tyukavina, A.; Thau, D.; Stehman,
463 S.V.; Goetz, S.J.; Loveland, T.R.; Kommareddy, A.; Egorov, A.; Chini, L.; Justice, C.O.; Townshend,
464 J.R.G. High-Resolution Global Maps of 21st-Century Forest Cover Change. *Science* **2013**, *342*, 850–853.
465 doi:10.1126/science.1244693.
- 466 2. Houghton, R.A.; House, J.I.; Pongratz, J.; van der Werf, G.R.; DeFries, R.S.; Hansen, M.C.; Le Quéré, C.;
467 Ramankutty, N. Carbon emissions from land use and land-cover change. *Biogeosciences* **2012**, *9*, 5125–5142.
468 doi:10.5194/bg-9-5125-2012.
- 469 3. Tyukavina, A.; Baccini, A.; Hansen, M.C.; Potapov, P.V.; Stehman, S.V.; Houghton, R.A.; Krylov, A.M.;
470 Turubanova, S.; Goetz, S.J. Aboveground carbon loss in natural and managed tropical forests from 2000 to
471 2012. *Environmental Research Letters* **2015**, *10*, 074002. doi:10.1088/1748-9326/10/7/074002.
- 472 4. van der Werf, G.R.; Morton, D.C.; DeFries, R.S.; Olivier, J.G.J.; Kasibhatla, P.S.; Jackson, R.B.; Collatz, G.J.;
473 Randerson, J.T. CO₂ emissions from forest loss. *Nature Geoscience* **2009**, *2*, 737–738. doi:10.1038/ngeo671.

- 474 5. Fauset, S.; Gloor, M.U.; Aidar, M.P.M.; Freitas, H.C.; Fyllas, N.M.; Marabesi, M.A.; Rochelle, A.L.C.;
475 Shenkin, A.; Vieira, S.A.; Joly, C.A. Tropical forest light regimes in a human-modified landscape. *Ecosphere*
476 **2017**, *8*, e02002. doi:10.1002/ecs2.2002.
- 477 6. Brinck, K.; Fischer, R.; Groeneveld, J.; Lehmann, S.; Dantas De Paula, M.; Pütz, S.; Sexton, J.O.; Song, D.;
478 Huth, A. High resolution analysis of tropical forest fragmentation and its impact on the global carbon
479 cycle. *Nature Communications* **2017**, *8*. doi:10.1038/ncomms14855.
- 480 7. Didham, R.K. Edge Structure Determines the Magnitude of Changes in Microclimate and Vegetation
481 Structure in Tropical Forest Fragments. *Biotropica* **1999**, *31*, 17–30.
- 482 8. Laurance, W.F.; Delamônica, P.; Laurance, S.G.; Vasconcelos, H.L.; Lovejoy, T.E. Rainforest fragmentation
483 kills big trees. *Nature* **2000**, *404*, 836–836. doi:10.1038/35009032.
- 484 9. Magnago, L.F.S.; Magrach, A.; Laurance, W.F.; Martins, S.V.; Meira-Neto, J.A.A.; Simonelli, M.; Edwards,
485 D.P. Would protecting tropical forest fragments provide carbon and biodiversity cobenefits under REDD+?
486 *Global Change Biology* **2015**, *21*, 3455–3468. doi:10.1111/gcb.12937.
- 487 10. Poorter, L.; Bongers, F. Leaf traits are good predictors of plant performance across 53 rain forest species.
488 *Ecology* **2006**, *87*, 1733–1743. doi:10.1890/0012-9658(2006)87[1733:LTAGPO]2.0.CO;2.
- 489 11. Barlow, J.; Lennox, G.D.; Ferreira, J.; Berenguer, E.; Lees, A.C.; Nally, R.M.; Thomson, J.R.; Ferraz, S.F.d.B.;
490 Louzada, J.; Oliveira, V.H.F.; Parry, L.; Ribeiro de Castro Solar, R.; Vieira, I.C.G.; Aragão, L.E.O.C.; Begotti,
491 R.A.; Braga, R.F.; Cardoso, T.M.; Jr, R.C.D.O.; Souza Jr, C.M.; Moura, N.G.; Nunes, S.S.; Siqueira, J.V.;
492 Pardini, R.; Silveira, J.M.; Vaz-de Mello, F.Z.; Veiga, R.C.S.; Venturieri, A.; Gardner, T.A. Anthropogenic
493 disturbance in tropical forests can double biodiversity loss from deforestation. *Nature* **2016**, *535*, 144–147.
494 doi:10.1038/nature18326.
- 495 12. Van de Perre, F.; Willig, M.R.; Presley, S.J.; Bapeamoni Andemwana, F.; Beeckman, H.; Boeckx, P.; Cooleman,
496 S.; de Haan, M.; De Kesel, A.; Dessein, S.; Grootaert, P.; Huygens, D.; Janssens, S.B.; Kearsley, E.; Kabeya,
497 P.M.; Leponce, M.; Van den Broeck, D.; Verbeeck, H.; Würsten, B.; Leirs, H.; Verheyen, E. Reconciling
498 biodiversity and carbon stock conservation in an Afrotropical forest landscape. *Science Advances* **2018**,
499 *4*, eaar6603. doi:10.1126/sciadv.aar6603.
- 500 13. Mitchard, E.T.A. The tropical forest carbon cycle and climate change. *Nature* **2018**, *559*, 527–534.
501 doi:10.1038/s41586-018-0300-2.
- 502 14. Ploton, P.; Pélassier, R.; Proisy, C.; Flavenot, T.; Barbier, N.; Rai, S.N.; Couteron, P. Assessing aboveground
503 tropical forest biomass using Google Earth canopy images. *Ecological Applications* **2012**, *22*, 993–1003.
- 504 15. Couteron, P.; Pelissier, R.; Nicolini, E.a.; Paget, D. Predicting tropical forest stand structure parameters
505 from Fourier transform of very high-resolution remotely sensed canopy images. *Journal of Applied Ecology*
506 **2005**, *42*, 1121–1128. doi:10.1111/j.1365-2664.2005.01097.x.
- 507 16. Barbier, N.; Couteron, P.; Proisy, C.; Malhi, Y.; Gastellu-Etchegorry, J.P. The variation of apparent crown
508 size and canopy heterogeneity across lowland Amazonian forests. *Global Ecology and Biogeography* **2010**,
509 *19*, 72–84. doi:10.1111/j.1466-8238.2009.00493.x.
- 510 17. DeFries, R.S.; Houghton, R.A.; Hansen, M.C.; Field, C.B.; Skole, D.; Townshend, J. Carbon emissions from
511 tropical deforestation and regrowth based on satellite observations for the 1980s and 1990s. *Proceedings of
512 the National Academy of Sciences* **2002**, *99*, 14256–14261. doi:10.1073/pnas.182560099.
- 513 18. Achard, F.; Beuchle, R.; Mayaux, P.; Stibig, H.J.; Bodart, C.; Brink, A.; Carboni, S.; Desclée, B.; Donnay, F.;
514 Eva, H.D.; Lupi, A.; Raši, R.; Seliger, R.; Simonetti, D. Determination of tropical deforestation rates and
515 related carbon losses from 1990 to 2010. *Global Change Biology* **2014**, *20*, 2540–2554. doi:10.1111/gcb.12605.
- 516 19. Ramankutty, N.; Foley, J.A. Estimating historical changes in global land cover: Croplands from 1700 to
517 1992. *Global Biogeochemical Cycles* **1999**, *13*, 997–1027. doi:10.1029/1999GB900046.
- 518 20. Sader, S.A.; Joyce, A.T. Deforestation Rates and Trends in Costa Rica, 1940 to 1983. *Biotropica* **1988**, *20*, 11.
519 doi:10.2307/2388421.
- 520 21. Willcock, S.; Phillips, O.L.; Platts, P.J.; Swetnam, R.D.; Balmford, A.; Burgess, N.D.; Ahrends, A.; Bayliss,
521 J.; Doggart, N.; Doody, K.; Fanning, E.; Green, J.M.H.; Hall, J.; Howell, K.L.; Lovett, J.C.; Marchant, R.;
522 Marshall, A.R.; Mbilinyi, B.; Munishi, P.K.T.; Owen, N.; Topp-Jorgensen, E.J.; Lewis, S.L. Land cover
523 change and carbon emissions over 100 years in an African biodiversity hotspot. *Global Change Biology* **2016**,
524 *22*, 2787–2800. doi:10.1111/gcb.13218.
- 525 22. Song, D.X.; Huang, C.; Sexton, J.O.; Channan, S.; Feng, M.; Townshend, J.R. Use of Landsat and
526 Corona data for mapping forest cover change from the mid-1960s to 2000s: Case studies from the Eastern

- United States and Central Brazil. *ISPRS Journal of Photogrammetry and Remote Sensing* **2015**, *103*, 81–92. doi:10.1016/j.isprsjprs.2014.09.005.
23. Nita, M.D.; Munteanu, C.; Gutman, G.; Abrudan, I.V.; Radeloff, V.C. Widespread forest cutting in the aftermath of World War II captured by broad-scale historical Corona spy satellite photography. *Remote Sensing of Environment* **2018**, *204*, 322–332. doi:10.1016/j.rse.2017.10.021.
24. Buitenwerf, R.; Bond, W.J.; Stevens, N.; Trollope, W.S.W. Increased tree densities in South African savannas: >50 years of data suggests CO₂ as a driver. *Global Change Biology* **2012**, *18*, 675–684. doi:10.1111/j.1365-2486.2011.02561.x.
25. Hudak, A.T.; Wessman, C.A. Textural Analysis of Historical Aerial Photography to Characterize Woody Plant Encroachment in South African Savanna. *Remote Sensing of Environment* **1998**, *66*, 317–330. doi:10.1016/S0034-4257(98)00078-9.
26. Frankl, A.; Seghers, V.; Stal, C.; De Maeyer, P.; Petrie, G.; Nyssen, J. Using image-based modelling (SfM-MVS) to produce a 1935 ortho-mosaic of the Ethiopian highlands. *International Journal of Digital Earth* **2015**, *8*, 421–430. doi:10.1080/17538947.2014.942715.
27. Nyssen, J.; Petrie, G.; Mohamed, S.; Gebremeskel, G.; Seghers, V.; Debever, M.; Hadgu, K.M.; Stal, C.; Billi, P.; Demaeyer, P.; Haile, M.; Frankl, A. Recovery of the aerial photographs of Ethiopia in the 1930s. *Journal of Cultural Heritage* **2016**, *17*, 170–178. doi:10.1016/j.culher.2015.07.010.
28. Lewis, S.L.; Lopez-Gonzalez, G.; Sonké, B.; Affum-Baffoe, K.; Baker, T.R.; Ojo, L.O.; Phillips, O.L.; Reitsma, J.M.; White, L.; Comiskey, J.A.; Djuiouo K, M.N.; Ewango, C.E.N.; Feldpausch, T.R.; Hamilton, A.C.; Gloor, M.; Hart, T.; Hladik, A.; Lloyd, J.; Lovett, J.C.; Makana, J.R.; Malhi, Y.; Mbago, F.M.; Ndangalasi, H.J.; Peacock, J.; Peh, K.S.H.; Sheil, D.; Sunderland, T.; Swaine, M.D.; Taplin, J.; Taylor, D.; Thomas, S.C.; Votere, R.; Wöll, H. Increasing carbon storage in intact African tropical forests. *Nature* **2009**, *457*, 1003–1006. Publisher: Earth and Biosphere Institute, School of Geography, University of Leeds, Leeds LS2 9JT, UK. s.l.lewis@leeds.ac.uk.
29. Butsic, V.; Baumann, M.; Shortland, A.; Walker, S.; Kuemmerle, T. Conservation and conflict in the Democratic Republic of Congo: The impacts of warfare, mining, and protected areas on deforestation. *Biological Conservation* **2015**, *191*, 266–273. doi:10.1016/j.biocon.2015.06.037.
30. Kearsley, E.; de Haulleville, T.; Hufkens, K.; Kidimbu, A.; Toirambe, B.; Baert, G.; Huygens, D.; Kebede, Y.; Defourny, P.; Bogaert, J.; Beeckman, H.; Steppe, K.; Boeckx, P.; Verbeeck, H. Conventional tree height-diameter relationships significantly overestimate aboveground carbon stocks in the Central Congo Basin. *Nature communications* **2013**, *4*, 2269. doi:10.1038/ncomms3269.
31. Lewis, S.L.; Maslin, M.A. Defining the Anthropocene. *Nature* **2015**, *519*, 171–180. doi:10.1038/nature14258.
32. Bauters, M.; Ampoorter, E.; Huygens, D.; Kearsley, E.; De Haulleville, T.; Sellan, G.; Verbeeck, H.; Boeckx, P.; Verheyen, K. Functional identity explains carbon sequestration in a 77-year-old experimental tropical plantation. *Ecosphere* **2015**, *6*, art198. doi:10.1890/ES15-00342.1.
33. Zuiderveld, K. Contrast Limited Adaptive Histogram Equalization. In *Graphics GEMs IV*; Academic Press: San Diego, CA, USA, 1994; pp. 474–485.
34. Ullman, S. The Interpretation of Structure from Motion. *Proceedings of the Royal Society of London. Series B, Biological Sciences* **1979**, *203*, 405–426.
35. QGIS Development team., QGIS Geographic Information System., 2018. Available at: <http://qgis.osgeo.org>.
36. Ronneberger, O.; Fischer, P.; Brox, T. U-Net: Convolutional Networks for Biomedical Image Segmentation. In *Medical Image Computing and Computer-Assisted Intervention – MICCAI 2015*; Navab, N.; Hornegger, J.; Wells, W.M.; Frangi, A.F., Eds.; Springer International Publishing: Cham, 2015; Vol. 9351, pp. 234–241. doi:10.1007/978-3-319-24574-4_28.
37. Chollet, F. Keras, 2015. Available at: <https://github.com/fchollet/keras>.
38. Yakubovskiy, P. Segmentation Models, 2019. Available at: https://github.com/qubvel/segmentation_models.
39. Martín Abadi.; Ashish Agarwal.; Paul Barham.; Eugene Brevdo.; Zhifeng Chen.; Craig Citro.; Greg S. Corrado.; Andy Davis.; Jeffrey Dean.; Matthieu Devin.; Sanjay Ghemawat.; Ian Goodfellow.; Andrew Harp.; Geoffrey Irving.; Michael Isard.; Jia, Y.; Rafal Jozefowicz.; Lukasz Kaiser.; Manjunath Kudlur.; Josh Levenberg.; Dandelion Mané.; Rajat Monga.; Sherry Moore.; Derek Murray.; Chris Olah.; Mike Schuster.; Jonathon Shlens.; Benoit Steiner.; Ilya Sutskever.; Kunal Talwar.; Paul Tucker.; Vincent Vanhoucke.; Vijay

- 580 Vasudevan.; Fernanda Viégas.; Oriol Vinyals.; Pete Warden.; Martin Wattenberg.; Martin Wicke.; Yuan Yu.;
581 Xiaoqiang Zheng. TensorFlow: Large-Scale Machine Learning on Heterogeneous Systems, 2015. Available
582 at: <https://www.tensorflow.org/>.
- 583 40. Kingma, D.P.; Ba, J. Adam: A Method for Stochastic Optimization. *arXiv:1412.6980 [cs]* **2017**. arXiv:
584 1412.6980.
- 585 41. Dice, L.R. Measures of the Amount of Ecologic Association Between Species. *Ecology* **1945**, *26*, 297–302.
586 doi:10.2307/1932409.
- 587 42. Dale, M.R.T. *Spatial pattern analysis in plant ecology*; Cambridge studies in ecology, Cambridge University
588 Press: Cambridge ; New York, 1999.
- 589 43. Hesselbarth, M.H.K.; Sciaini, M.; With, K.A.; Wiegand, K.; Nowosad, J. landscapemetrics: an open-source
590 R tool to calculate landscape metrics. *Ecography* **2019**.
- 591 44. Li, B.L. Fractal geometry applications in description and analysis of patch patterns and patch dynamics.
592 *Ecological Modelling* **2000**, *132*, 33–50. ISBN: Ecol. Model.
- 593 45. Mandelbrot, B.B. *Fractals: Form, Chance and Dimension*; W.H. Freeman and co.: New York, US, 1977.
- 594 46. Bustillo, E.; Raets, L.; Beeckman, H.; Bourland, N.; Rousseau, M.; Hubau, W.; De Mil, T. Evaluation du
595 potentiel énergétique de la biomasse aérienne ligneuse des anciennes plantations de l'INERA Yangambi.
596 Technical report, CIFOR, 2018.
- 597 47. Couteron, P. Quantifying change in patterned semi-arid vegetation by Fourier analysis of digitized aerial
598 photographs. *International Journal of Remote Sensing* **2002**, *23*, 3407–3425. doi:10.1080/01431160110107699.
- 599 48. Wilcoxon, F. Individual comparisons by ranking methods. *Biometrics* **1945**, *1*, 80–83.
- 600 49. Kadmon, R.; Harari-Kremer, R. Studying Long-Term Vegetation Dynamics Using Digital
601 Processing of Historical Aerial Photographs. *Remote Sensing of Environment* **1999**, *68*, 164–176.
602 doi:10.1016/S0034-4257(98)00109-6.
- 603 50. Peres, C.A.; Barlow, J.; Laurance, W.F. Detecting anthropogenic disturbance in tropical forests. *Trends in
604 Ecology & Evolution* **2006**, *21*, 227–229. doi:10.1016/j.tree.2006.03.007.
- 605 51. Verhoeven, G. BRDF and its Impact on Aerial Archaeological Photography: BRDF and its impact on aerial
606 archaeological photography. *Archaeological Prospection* **2017**, *24*, 133–140. doi:10.1002/arp.1559.
- 607 52. Park, J.Y.; Muller-Landau, H.C.; Lichstein, J.W.; Rifai, S.W.; Dandois, J.P.; Bohlman, S.A. Quantifying Leaf
608 Phenology of Individual Trees and Species in a Tropical Forest Using Unmanned Aerial Vehicle (UAV)
609 Images. *Remote Sensing* **2019**, *11*, 1534. doi:10.3390/rs11131534.
- 610 53. Simini, F.; Anfodillo, T.; Carrer, M.; Banavar, J.R.; Maritan, A. Self-similarity and scaling
611 in forest communities. *Proceedings of the National Academy of Sciences* **2010**, *107*, 7658–7662.
612 doi:10.1073/pnas.1000137107.
- 613 54. Sole, R.V.; Manrubia, S.C. Self-similarity in rain forests: evidence for a critical state. *Physical Review E* **1995**,
614 *51*, 6250 – 6253.
- 615 55. Hughes, M.L.; McDowell, P.F.; Marcus, W.A. Accuracy assessment of georectified aerial photographs:
616 Implications for measuring lateral channel movement in a GIS. *Geomorphology* **2006**, *74*, 1–16.
617 doi:10.1016/j.geomorph.2005.07.001.
- 618 56. Buscombe, D.; Ritchie, A. Landscape Classification with Deep Neural Networks. *Geosciences* **2018**, *8*, 244.
619 doi:10.3390/geosciences8070244.
- 620 57. Gascon, C.; Williamson, G.B.; Fonseca, G.A.B.d. Receding Forest Edges and Vanishing Reserves. *Science,
621 New Series* **2000**, *288*, 1356–1358.
- 622 58. Phillips, O.L.; Rose, S.; Mendoza, A.M.; Vargas, P.N. Resilience of Southwestern Amazon Forests to
623 Anthropogenic Edge Effects. *Conservation Biology* **2006**, *20*, 1698–1710. doi:10.1111/j.1523-1739.2006.00523.x.
- 624 59. Reinmann, A.B.; Hutyra, L.R. Edge effects enhance carbon uptake and its vulnerability to climate
625 change in temperate broadleaf forests. *Proceedings of the National Academy of Sciences* **2017**, *114*, 107–112.
626 doi:10.1073/pnas.1612369114.
- 627 60. Arima, E.Y.; Walker, R.T.; Perz, S.; Souza, C. Explaining the fragmentation in the Brazilian Amazonian
628 forest. *Journal of Land Use Science* **2015**, pp. 1–21. doi:10.1080/1747423X.2015.1027797.
- 629 61. Arima, E.Y.; Barreto, P.; Araújo, E.; Soares-Filho, B. Public policies can reduce tropical deforestation: Lessons
630 and challenges from Brazil. *Land Use Policy* **2014**, *41*, 465–473. doi:10.1016/j.landusepol.2014.06.026.
- 631 62. Larson, A.M. Forest tenure reform in the age of climate change: Lessons for REDD+. *Global Environmental
632 Change* **2011**, *21*, 540–549. doi:10.1016/j.gloenvcha.2010.11.008.

- 633 63. Gourlet-Fleury, S.; Mortier, F.; Fayolle, A.; Baya, F.; Ouédraogo, D.; Bénédet, F.; Picard, N. Tropical forest
634 recovery from logging: a 24 year silvicultural experiment from Central Africa. *Philosophical Transactions of*
635 *the Royal Society B: Biological Sciences* **2013**, *368*, 20120302. doi:10.1098/rstb.2012.0302.
- 636 64. Solórzano, J.V.; Gallardo-cruz, J.A.; González, E.J.; Peralta-carreta, C.; Hernández-gómez, M.; Oca,
637 A.F.m.D.; Cervantes-jiménez, L.G.; Solórzano, J.V.; Gallardo-cruz, J.A.; González, E.J.; Peralta-carreta,
638 C.; Hernández-gómez, M.; Oca, A.F.m.D.; Cervantes-jiménez, L.G. Contrasting the potential of
639 Fourier transformed ordination and gray level co-occurrence matrix textures to model a tropical swamp
640 forest 's structural and diversity attributes. *Journal of Applied Remote Sensing* **2018**, *12*, 036006.
641 doi:10.1111/1.JRS.12.036006.
- 642 65. R Core Team. *R: A Language and Environment for Statistical Computing*; R Foundation for Statistical
643 Computing: Vienna, Austria, 2019.
- 644 66. Hijmans, R.J. raster: Geographic Data Analysis and Modeling, 2019. Available at: <https://CRAN.R-project.org/package=raster>.
- 645 67. Leutner, B.; Horning, N.; Schwalb-Willmann, J. RStoolbox: Tools for Remote Sensing Data Analysis, 2019.
646 Available at: <https://CRAN.R-project.org/package=RStoolbox>.
- 647 68. Wickham, H. tidyverse: Easily Install and Load the 'Tidyverse', 2017. Available at: <https://CRAN.R-project.org/package=tidyverse>.
- 648 69. Arnold, J.B. ggthemes: Extra Themes, Scales and Geoms for 'ggplot2', 2019. Available at: <https://CRAN.R-project.org/package=ggthemes>.
- 649 70. Wickham, H. scales: Scale Functions for Visualization, 2018. Available at: <https://CRAN.R-project.org/package=scales>.
- 650 71. Wilke, C.O. cowplot: Streamlined Plot Theme and Plot Annotations for 'ggplot2', 2019. Available at:
651 <https://CRAN.R-project.org/package=cowplot>.
- 652 72. Pebesma, E. Simple Features for R: Standardized Support for Spatial Vector Data. *The R Journal* **2018**,
653 *10*, 439–446. doi:10.32614/RJ-2018-009.
- 654 73. South, A. rnaturalearth: World Map Data from Natural Earth, 2017. Available at: <https://CRAN.R-project.org/package=rnaturalearth>.

655 © 2020 by the authors. Submitted to *Remote Sens.* for possible open access publication
656 under the terms and conditions of the Creative Commons Attribution (CC BY) license
657 (<http://creativecommons.org/licenses/by/4.0/>).